Non-Contact Capacitive-Coupling-Based and Magnetic-Field-Sensing-Assisted Technique for Monitoring Voltage of Overhead Power Transmission Lines

Ke Zhu, Wing Kin Lee, *Member, IEEE*, and Philip W. T. Pong, *Senior Member, IEEE*

Abstract—Adopting non-contact capacitive coupling for voltage monitoring is promising as it avoids electrical connection with high-voltage transmission lines. However, coupled voltage transformation matrix to correlate voltage of overhead transmission lines and induction bars has not been achieved mathematically due to the lack of equivalent electric circuit model for analyzing the physical phenomenon. Moreover, exact spatial positions of overhead transmission lines are typically unknown and dynamic in practice. In this paper, a technique based on non-contact capacitive-coupling and assisted by magnetic-field sensing for monitoring voltage of overhead transmission lines was designed and implemented. The technique in this paper is demonstrated on a single-circuit transmission line as an example, while it is also applicable for multi-circuit transmission lines. The capacitive coupling between overhead transmission lines and induction bars were modeled as lumped capacitors, and then, the equivalent electric circuit model was established. The coupled voltage transformation matrix to correlate voltage of overhead transmission lines and induced voltage of induction bars mathematically was formed accordingly. This paper was also carried out to analyze the effect of ground wires, sensitivity of induction bars, the ability of high-frequency transient measurement, and the intrinsic capacitance of a measurement instrument. The exact spatial positions of overhead transmission lines were acquired by integrating magnetic-field sensing with the stochastic optimization algorithm. The methodology was verified by simulation on the 10-kV single-circuit three-phase overhead transmission lines taking non-ideality of signal measurement in account, and wavelet de-noising algorithm was supplemented to filter the interferences. A scaled testbed to experiment the technique was built to monitor 220 V overhead transmission lines in the lab, and also the typical waveform of a high-frequency switching surge (up to 1 kHz), which was generated by a programmable ac source. The reconstructed results match well with the actual values. This technique can largely improve transient-fault identification over traditional potential transformers by the virtue of the increased upper measurement limit and bandwidth through capacitive coupling. Moreover, it can be implemented with low-cost copper induction bars and compact magnetoresistive sensors, enabling large-scale application to realize sectional monitoring in the wide area.

Index Terms—Capacitive coupling, magnetic-field sensing, voltage monitoring, overhead transmission lines.

I. INTRODUCTION

OVERHEAD transmission lines are used to transmit electric power over long distances. Faults can occur at overhead transmission lines due to environmental impact, resulting in variation of voltage amplitude and frequency [1]. Power fluctuation from uncertain renewable energy can also introduce more transient voltage disturbances [2]. Therefore, it is important to monitor voltage of overhead transmission lines for reliability and stability assessment and to extract useful information such as fault type, fault location and fault duration so that relay protection can be coordinated [3].

The main challenges for transmission-grid monitoring are in terms of measuring voltage amplitude and frequency [4]–[6]. As more extra-high voltage AC (330 kV to 765 kV) and ultra-high voltage AC (1,000 kV) transmission lines are being constructed to cover larger geographical area, measuring instruments need to be able to measure voltage with higher upper limit. Wider frequency bandwidth should be addressed not only to detect high frequency response such as transient fault (possibly MHz), but also the emerging high-voltage DC (HVDC) transmission grids [7]. In addition, sectional monitoring ability is indispensable because overhead transmission lines covering large area are exposed to varied and complicated environment. When an incident occurs at a certain point of a large transmission network, remedial actions such as disconnection and reclosing should be taken timely in order to avoid spreading and endangering the rest of the grid. Traditionally, voltage monitoring relies on potential transformers (PTs) measuring overhead busbars inside substations. Unfortunately, traditional PTs cannot meet the above measurement requirements [8]. Due to saturation in magnetic cores, operation exceeding 10% of the rated voltage can cause serious measurement errors and heating. Thus PTs fail to measure transient faults which can be much higher than the rated. Moreover, magnetic core restricts the frequency bandwidth in

the range from tens of Hz to kHz. Considering the necessary galvanical connection to the high-voltage live wires and expensive ferromagnetic material and insulation, PTs are unlikely to be deployable in large scale for realizing sectional monitoring.

The capacitive-coupling phenomenon is promising for non-contact voltage monitoring of overhead transmission lines and shows many advantages over traditional PTs [9]–[11]. In the large mountainous and uninhabited areas, the high-voltage (e.g., 10, 35, 110, 220, 500 and 800 kV) overhead transmission lines are the greatest source to induce voltages on induction bars by the time-varying electric field emanated from power lines [12], [13]. The induced voltage on induction bars results from the time-varying electric field emanated from power lines. Without galvanical connection of magnetic core, magnetic saturation and heating are avoided. Through capacitive coupling, the induced voltage on induction bars are stepped down and measured. As such, serious overvoltage in fault incident is possible to be detected in a way without exceeding measurement range. The induced voltage on induction bars through capacitive coupling responds from DC to MHz [14] and can be measured by voltage-sensing devices such as oscilloscopes or multimeters. The induction bars can be fabricated from low-cost metallic materials. Its non-contact detection nature eliminates electrical hazards to the workers and greatly facilitates its large-scale deployment and installation.

However, this detection principle has not been developed into practice because of the following reasons though capacitive coupling between overhead transmission lines and induction bars has been observed for quite a long time [15]. Firstly, the coupled voltage transformation matrix that correlates mathematically between the voltage of overhead transmission lines and the induced voltage of induction bars has not been derived since an equivalent electric circuit model is not available for modelling and analyzing the physical phenomenon. Moreover, when induced voltage on induction bars are measured in reality, its electrical configuration is altered and further complicated by the additional capacitance introduced by the measuring instrument [16]–[18]. Thirdly, relative positions between overhead transmission lines and induction bars are not easy to acquire in reality because the transmission lines are well above ground and they are not necessarily static due to atmospheric disturbances such as wind.

In this paper, a technique based on the non-contact capacitive-coupling and assisted by magnetic-field sensing for monitoring voltage of overhead transmission lines was proposed. The technique in the paper is demonstrated on a single-circuit transmission line as an example while it is also applicable for multi-circuit transmission lines. The capacitive coupling between overhead transmission lines and induction bars was modeled as lumped capacitors, and the equivalent electric circuit model was established accordingly. Through analyzing the circuit, the coupled voltage transformation matrix to correlate the voltage of overhead transmission lines and the induced voltage of induction bars mathematically was formed. The study was also carried out to analyze the effect of ground wires, sensitivity of induction bars, the ability of high-frequency transient measurement, and intrinsic capacitance introduced by an measurement instrument on the equivalent
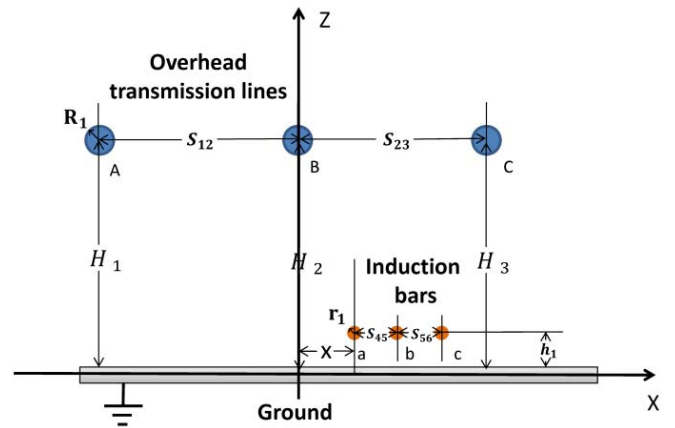

Fig. 1. Geometric configuration of overhead transmission lines and induction bars.

electric circuit model and coupled voltage transformation matrix. Based on our previous work [19], a magnetic-sensing-based technique was developed that can reconstruct position of overhead transmission lines from the measured magnetic field emanated from the overhead transmission lines through the stochastic optimization algorithm. Wavelet de-noising algorithm was further integrated to tackle non-idealities of measured signals due to either background interferences or intrinsic noise of sensing devices. The corresponding sensing platform was proposed and demonstrated in normal and faulty conditions respectively by simulation on a 10 kV single-circuit three-phase overhead transmission lines. A scaled testbed to experiment the technique was built to monitor 220 V overhead transmission lines in the lab, and also the typical waveform of a high-frequency switching surge which was generated by a programmable AC source. The reconstructed results match well with the actual values. The non-contact technique is competent for monitoring voltage of overhead transmission lines without interrupting the operating circuit. The compact size, reduced cost and the non-galvanical connection features compared to PTs enable the platform to be installed in large-scale to improve situation awareness.

II. CAPACITIVE COUPLING BETWEEN OVERHEAD TRANSMISSION LINES AND INDUCTION BARS

A. Capacitance Calculation

Overhead transmission lines carrying three-phase power can be configured as either single- or multi- circuit [4], [20], [21]. Multiple circuits are used for transferring more power over a particular distance with less cost for constructing extra transmission towers. The technique is firstly demonstrated on a single-circuit transmission line, and a graph illustrating the geometric relation between single-circuit overhead transmission lines and induction bars is shown in Fig. 1. The altitude of each conductor (phase A, B and C) of the three-phase transmission line are H_1, H_2, and H_3 respectively, and the induction bars (bar a, b and c) are located at an altitude of h_1 above the ground. The spatial distances between adjacent conductors of overhead transmission lines (induction bars) are S_{12} and S_{23} (S_{45} and S_{56}), respectively. The radii of overhead
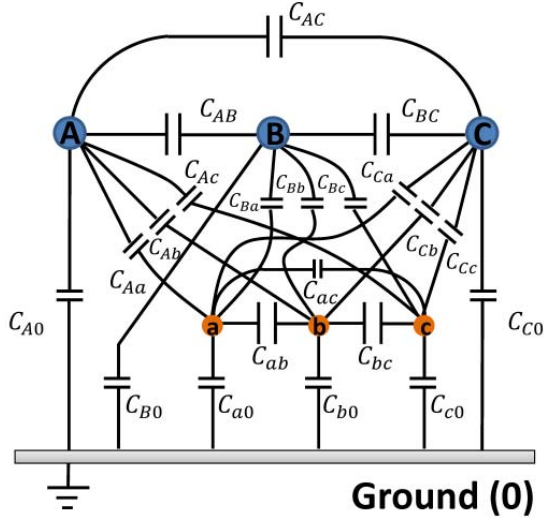
Fig. 2. Lumped capacitors formed for overhead transmission lines and induction bars.

transmission lines (induction bars) are $R_1 (r_1)$. The horizontal distance between phase B (overhead transmission line) and bar a (induction bar) is x.

The capacitive coupling within the network is treated as a lumped capacitor between objects. The time-varying voltage of overhead transmission lines are the source while the induction bars are the receivers as they are the objects being affected. The lumped capacitors formed are shown in Fig. 2. The calculation model is based on isolated multi-conductor system, and the electrical field distribution only depends on conductor shape, dimensions, and relative positions of objects. All the electric field lines start and end in the conductors within the system.

In this model, the overhead transmission lines and the induction bars are aligned along the same direction. The phase voltage of phase A, B and C on the overhead transmission lines at a certain time point t are denoted as $V_A(t)$, $V_B(t)$ and $V_C(t)$ and the corresponding electric charges are $Q_A(t)$, $Q_B(t)$ and $Q_C(t)$. Similarly, the phase voltage and the corresponding electric charges of induction bar a, b, c are denoted as $V_a(t)$, $V_b(t)$, $V_c(t)$, $Q_a(t)$, $Q_b(t)$ and $Q_c(t)$. Then the voltages in this isolated system can be related by

$$\begin{pmatrix} V_A(t) \\ V_B(t) \\ V_C(t) \\ V_a(t) \\ V_b(t) \\ V_c(t) \end{pmatrix} = \begin{pmatrix} \alpha_{11} & \alpha_{12} & \alpha_{13} & \alpha_{14} & \alpha_{15} & \alpha_{16} \\ \alpha_{21} & \alpha_{22} & \alpha_{23} & \alpha_{24} & \alpha_{25} & \alpha_{26} \\ \alpha_{31} & \alpha_{32} & \alpha_{33} & \alpha_{34} & \alpha_{35} & \alpha_{36} \\ \alpha_{41} & \alpha_{42} & \alpha_{43} & \alpha_{44} & \alpha_{45} & \alpha_{46} \\ \alpha_{51} & \alpha_{52} & \alpha_{53} & \alpha_{54} & \alpha_{55} & \alpha_{56} \\ \alpha_{61} & \alpha_{62} & \alpha_{63} & \alpha_{64} & \alpha_{65} & \alpha_{66} \end{pmatrix} \begin{pmatrix} Q_A(t) \\ Q_B(t) \\ Q_C(t) \\ Q_a(t) \\ Q_b(t) \\ Q_c(t) \end{pmatrix}$$

$$(1)$$

where α_{ij} ($i = 1, 2, \ldots, 6$; $j = 1, 2, \ldots, 6$) are potential coefficients depending on conductor shape, relative positions of the conductors and the permittivity of the surrounding medium. For $i = j$, the coefficient is called self-potential coefficient. For $i \neq j$, the coefficient is named mutual-potential coefficient. By means of image charge method, the potential coefficients can be expressed in terms of

conductor radius, altitude, their relative distance and image distance. For example, the self-potential coefficient α_{11} and mutual-potential coefficient α_{41} can be calculated as

$$\alpha_{11} = \frac{1}{2\pi \varepsilon_0} ln \frac{2H_1}{R_1} \tag{2}$$

$$\alpha_{41} = \frac{1}{2\pi \varepsilon_0} ln \frac{\sqrt{(s_{12} + x)^2 + (H_1 + h)2}}{\sqrt{(s_{12} + x)^2 + (H_1 - h)2}} \tag{3}$$

By taking inverse of the potential coefficient matrix in Eq. (1),

$$\begin{pmatrix} Q_A(t) \\ Q_B(t) \\ Q_C(t) \\ Q_a(t) \\ Q_b(t) \\ Q_c(t) \end{pmatrix} = \begin{pmatrix} \beta_{11} & \beta_{12} & \beta_{13} & \beta_{14} & \beta_{15} & \beta_{16} \\ \beta_{21} & \beta_{22} & \beta_{23} & \beta_{24} & \beta_{25} & \beta_{26} \\ \beta_{31} & \beta_{32} & \beta_{33} & \beta_{34} & \beta_{35} & \beta_{36} \\ \beta_{41} & \beta_{42} & \beta_{43} & \beta_{44} & \beta_{45} & \beta_{46} \\ \beta_{51} & \beta_{52} & \beta_{53} & \beta_{54} & \beta_{55} & \beta_{56} \\ \beta_{61} & \beta_{62} & \beta_{63} & \beta_{64} & \beta_{65} & \beta_{66} \end{pmatrix} \begin{pmatrix} V_A(t) \\ V_B(t) \\ V_C(t) \\ V_a(t) \\ V_b(t) \\ V_c(t) \end{pmatrix}$$

$$(4)$$

where β_{ij} ($i = 1, 2, \ldots, 6$; $j = 1, 2, \ldots, 6$) are called induction coefficients. For $i = j$, the coefficient is called self-inductance coefficient. For $i \neq j$, the coefficient is called mutual-inductance coefficient. Then the unit capacitance can be calculated with inductance coefficients. The unit capacitance between a conductor and the ground (self-capacitance) can be calculated as summation of each row in Eq. (4) of the induction coefficient matrix. For example, the self-capacitance of phase A is calculated as $C_{A0} = \beta_{11} + \beta_{12} + \ldots + \beta_{16}$, and the same for the others (C_{B0}, C_{C0}, C_{a0}, C_{b0} and C_{c0}). Unit capacitance C_{mn} (m =A, B, C and n= a, b, c) between conductors is called mutual-capacitance and it is calculated as

$$C_{mn} = -\beta_{ij}, \quad i = \begin{cases} 1, m = A \\ 2, m = B \\ 3, m = C, \end{cases} \quad j = \begin{cases} 4, n = a \\ 5, n = b \\ 6, n = c \end{cases} \tag{5}$$

By multiplying unit capacitance with length of the overlapping part between the two conductors, the total capacitance can be obtained.

It should be noted that the capacitance calculation is very straightforward when the directions of overhead transmission lines and induction bars are aligned. However, their directions do not necessarily be aligned in reality. In addition, the sagging and galloping of overhead transmission lines can happen. In these relatively complicated scenarios, finite-element method (FEM) can be deployed to calculate the capacitance in three-dimensional geometrical configuration.

B. Coupled Voltage Transformation Matrix

The equivalent electric circuit model for calculating induced voltage on induction bars is similar to [22] in which the induced voltages by 22 kV three-phase overhead power lines were determined. The delta-star transformation is implemented for star connection between overhead transmission lines and inductors bars. The transformed capacitors are shown in Fig. 3,
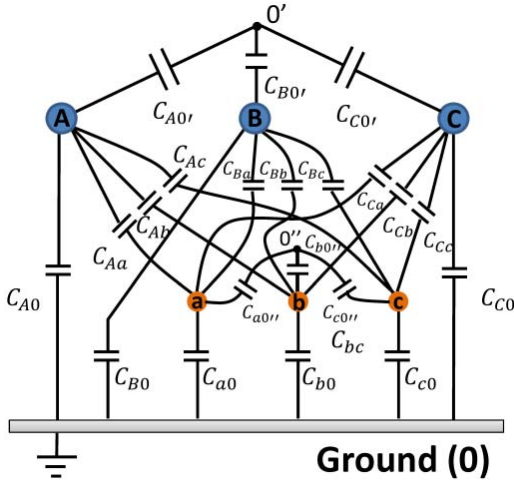
Fig. 3. Capacitors formed between overhead transmission lines and induction bars after delta-star transformation.
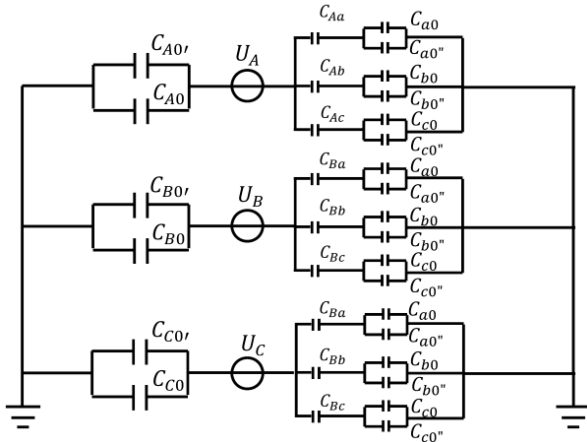

Fig. 4. Equivalent electric circuit model between overhead transmission lines and induction bars formed by capacitors.

and their capacitance can be calculated as

$$\frac{1}{C_{A0'}} = \frac{\frac{1}{C_{AB}} \cdot \frac{1}{C_{AC}}}{\frac{1}{C_{AB}} + \frac{1}{C_{AC}} + \frac{1}{C_{BC}}} \tag{6.1}$$

$$\frac{1}{C_{B0'}} = \frac{\frac{1}{C_{AB}} \cdot \frac{1}{C_{BC}}}{\frac{1}{C_{AB}} + \frac{1}{C_{AC}} + \frac{1}{C_{BC}}} \tag{6.2}$$

$$\frac{1}{C_{C0'}} = \frac{\frac{1}{C_{BC}} \cdot \frac{1}{C_{AC}}}{\frac{1}{C_{AB}} + \frac{1}{C_{AC}} + \frac{1}{C_{BC}}} \tag{6.3}$$

$$\frac{1}{C_{a0''}} = \frac{\frac{1}{C_{ab}} \cdot \frac{1}{C_{ac}}}{\frac{1}{C_{ab}} + \frac{1}{C_{ac}} + \frac{1}{C_{bc}}} \tag{7.1}$$

$$\frac{1}{C_{b0''}} = \frac{\frac{1}{C_{ab}} \cdot \frac{1}{C_{bc}}}{\frac{1}{C_{ab}} + \frac{1}{C_{ac}} + \frac{1}{C_{bc}}} \tag{7.2}$$

$$\frac{1}{C_{c0''}} = \frac{\frac{1}{C_{bc}} \cdot \frac{1}{C_{ac}}}{\frac{1}{C_{ab}} + \frac{1}{C_{ac}} + \frac{1}{C_{bc}}} \tag{7.3}$$

By transforming the capacitors of delta-connected phases (Fig. 2) into equivalent capacitors of star connection (Fig. 3), the null potentials of two star connections are equal with null potential of earth [22]. The equivalent electric circuit model consisting of lumped capacitors is shown in Fig. 4,
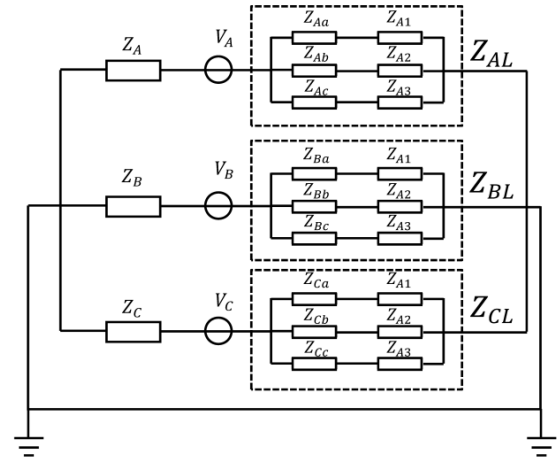

Fig. 5. Equivalent electric circuit model between overhead transmission lines and induction bars formed by impedance.

and it is expressed in terms of impedance in Fig. 5 for easier illustration.

The voltage of overhead transmission lines (V_A, V_B, V_C) and induction bars (V_a, V_b, V_c) can then be related as

$$
\begin{bmatrix} V_a \\ V_b \\ V_c \end{bmatrix} = \begin{bmatrix} \frac{Z_{A1}}{Z_{Aa}+Z_{A1}} & \frac{Z_{A1}}{Z_{Ba}+Z_{A1}} & \frac{Z_{A1}}{Z_{Ca}+Z_{A1}} \\ \frac{Z_{A2}}{Z_{Ab}+Z_{A2}} & \frac{Z_{A2}}{Z_{Bb}+Z_{A2}} & \frac{Z_{A2}}{Z_{Cb}+Z_{A2}} \\ \frac{Z_{A3}}{Z_{Ac}+Z_{A3}} & \frac{Z_{A3}}{Z_{Bc}+Z_{A3}} & \frac{Z_{A3}}{Z_{Cc}+Z_{A3}} \end{bmatrix} \begin{bmatrix} \frac{V_A}{Z_A+Z_{AL}}Z_{AL} \\ \frac{V_B}{Z_B+Z_{BL}}Z_{BL} \\ \frac{V_C}{Z_C+Z_{CL}}Z_{CL} \end{bmatrix}
$$

$$
= \begin{bmatrix} \frac{Z_{A1}}{Z_{Aa}+Z_{A1}} & \frac{Z_{A1}}{Z_{Ba}+Z_{A1}} & \frac{Z_{A1}}{Z_{Ca}+Z_{A1}} \\ \frac{Z_{A2}}{Z_{Ab}+Z_{A2}} & \frac{Z_{A2}}{Z_{Bb}+Z_{A2}} & \frac{Z_{A2}}{Z_{Cb}+Z_{A2}} \\ \frac{Z_{A3}}{Z_{Ac}+Z_{A3}} & \frac{Z_{A3}}{Z_{Bc}+Z_{A3}} & \frac{Z_{A3}}{Z_{Cc}+Z_{A3}} \end{bmatrix}
$$

$$
\times \begin{bmatrix} \frac{Z_{AL}}{Z_A+Z_{AL}} & 0 & 0 \\ 0 & \frac{Z_{BL}}{Z_B+Z_{BL}} & 0 \\ 0 & 0 & \frac{Z_{CL}}{Z_C+Z_{CL}} \end{bmatrix} \begin{bmatrix} V_A \\ V_B \\ V_C \end{bmatrix}
$$

$$
= AB \begin{bmatrix} V_A \\ V_B \\ V_C \end{bmatrix} \tag{8}
$$

where

$$
A = \begin{bmatrix} \frac{Z_{A1}}{Z_{Aa}+Z_{A1}} & \frac{Z_{A1}}{Z_{Ba}+Z_{A1}} & \frac{Z_{A1}}{Z_{Ca}+Z_{A1}} \\ \frac{Z_{A2}}{Z_{Ab}+Z_{A2}} & \frac{Z_{A2}}{Z_{Bb}+Z_{A2}} & \frac{Z_{A2}}{Z_{Cb}+Z_{A2}} \\ \frac{Z_{A3}}{Z_{Ac}+Z_{A3}} & \frac{Z_{A3}}{Z_{Bc}+Z_{A3}} & \frac{Z_{A3}}{Z_{Cc}+Z_{A3}} \end{bmatrix}
$$

$$
B = \begin{bmatrix} \frac{Z_{AL}}{Z_A+Z_{AL}} & 0 & 0 \\ 0 & \frac{Z_{BL}}{Z_B+Z_{BL}} & 0 \\ 0 & 0 & \frac{Z_{CL}}{Z_C+Z_{CL}} \end{bmatrix}
$$

Eq. (8) describes the relation between the phase voltage of the overhead transmission lines and the induced voltage of the induction bars. If the voltage on the induction bars can be measured in real time, the phase voltage of the overhead transmission lines can be derived simultaneously by solving Eq. (8):

$$
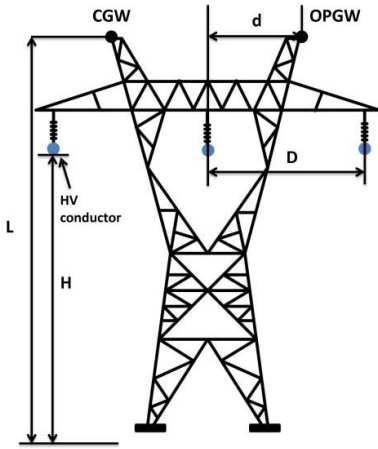\begin{bmatrix} V_A \\ V_B \\ V_C \end{bmatrix} = B^{-1}A^{-1} \begin{bmatrix} V_a \\ V_b \\ V_c \end{bmatrix} \tag{9}
$$

Fig. 6. Single-circuit lattice tower with the CGW and OPGW: altitude of overhead transmission lines (H), 20 m; altitude of the CGW and OPGW (L), 23 m; spacing distance between overhead transmission lines (D), 10 m; spacing distance between the central line and CGW (OPGW) (d), 2 m.

Fig. 8. Induced voltages on induction bars calculated analytically (lines) and by FEM (markers).
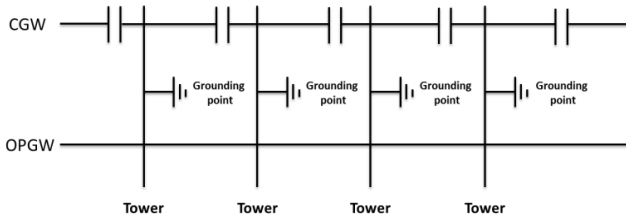

Fig. 7. Grounding method of CGW and OPGW for overhead transmission lines.

C. Effect of Ground Wires

The model established by Eq. (9) only involves the overhead transmission lines and induction bars. In fact, overhead transmission lines are often equipped with ground wires to minimize the likelihood of direct lightning strikes to phase conductors [23], or to serve as a parallel path with the earth for fault currents [24]. Therefore, the effects of the ground wires on induced voltage of induction bars are evaluated as follows.

The popular single-circuit lattice tower structure [25] was studied as an example (Fig. 6). Apart from the single-circuit structure of three-phase conductors, one common ground wire (CGW) and one optical fiber composite ground wire (OPGW) are installed above the transmission lines considering the lightning protection and communication [26]. The CGW is insulated with only one point grounded while the OPGW is grounded at each tower (Fig. 7) [27], [28]. The FEM simulation was conducted for evaluating the effects of the CGW and OPGW on induced voltages. In the simulation, each phase voltage of the three-phase transmission line was set to be 10 kV at 50 Hz. The three paralleled induction bars were installed with 1 m altitude and 2 m spacing distance with induction bar *b* under the phase B of overhead transmission lines (refer to Fig. 1). The induced voltages of the induction bars in a cycle were analytically calculated by Eq. (9), and the FEM results for the induced voltages with and without the CGW and OPGW are shown in Fig. 8. The induced voltages
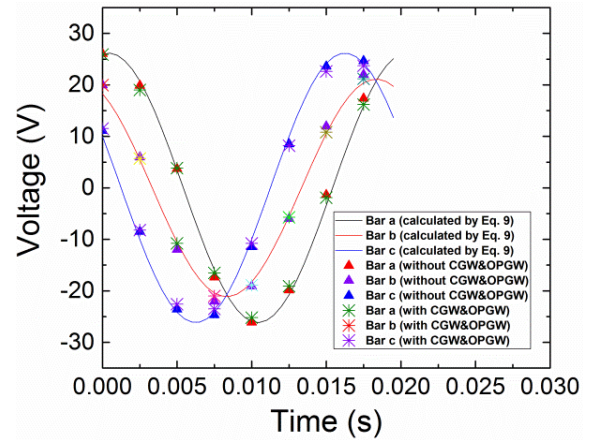
simulated by FEM without the CGW and OPGW match well with the analytical calculation, verifying the derived voltage relation between the overhead transmission lines and induction bars by Eq. (9). Moreover, the FEM results show that the induced voltages with and without the CGW and OPGW are almost the same (the small errors are caused by grid meshing in FEM), illustrating that the CGW and OPGW do not affect the induced voltages of induction bars indicated by Eq. (9). This is because the voltages on induction bars are induced by electrical fields, while the installation of the CGW and OPGW does not affect the electric field distribution under three-phase overhead transmission lines (i.e., the induction bars at the ground level). Therefore, Eq. (9) relating three-phase transmission lines and induction bars is applicable for the transmission tower installed with the CGW and OPGW.

It should be noted that due to the electromagnetic induction between ground wires and conductor wires, the voltages are also induced on the CGW and OPGW. Since the OPGW is grounded at each tower, a closed circuit is formed and the induced current would flow on the OPGW [29]. Apparently, the induced current generates extra magnetic fields besides those from the current-carrying phase conductors. Nevertheless, since the induced current on OPGW is only around ten amperes regarding a rated phase current of 1000 A (i.e. merely 1% of the rated phase current) [29], the extra generated magnetic fields would be extremely insignificant compared to those from the phase conductors. As such, the voltage monitoring for transmission lines based on the phase position reconstruction from measuring the magnetic fields (Section III(A)) is still of high accuracy.

D. Sensor Sensivitiy

Induced voltages of induction bars alter at various spatial locations. In our setup, the sensitivity (a ratio of the magnitude of the response to the magnitude of the quantity measured [30], [31]) for three induction bars are defined as

$$S_a = \frac{V_a}{V_A}, \quad S_b = \frac{V_b}{V_B}, \quad S_c = \frac{V_c}{V_C} \quad (10)$$
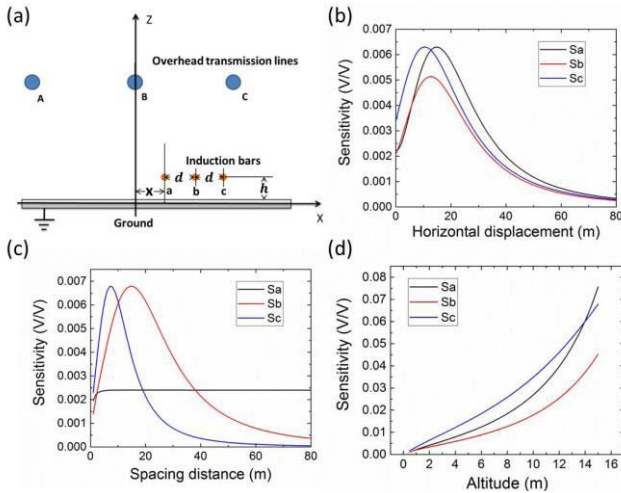
Fig. 9. Sensitivity of induction bars under various configurations of induction bars. (a) Adjustment of horizontal displacement (x), spacing distance (d), and height (h) under altitude (spacing) of overhead transmission lines are 20 m (10 m). (b) Sensitivity under various horizontal displacement. (c) Sensitivity under various spacing distances. (d) Sensitivity under various altitudes.

where S_a, S_b, S_c are the sensitivity of induction bar a, b, and c, V_a, V_b, V_c are the peak values of induced voltage of induction bars, and V_A, V_B, V_C are the peak values of three-phase voltage, respectively. The better sensitivity can enhance the performance of the proposed platform. Therefore, the sensitivity of three induction bars under various configurations, i.e., horizontal displacement (x), spacing distance (d), and altitude (h) were studied based on the model in Fig. 9 (a) as following:

1) Horizontal displacement: the induced voltages of induction bars were calculated by adjusting their horizontal displacement while fixing the altitude and spacing distance. The induction bars of 1 m altitude were spaced by 2 m, and the induction bars were simultaneously moved with various horizontal displacement in the simulation (x was set from 0 to 80 m). The sensitivity for three induction bars under various horizontal displacement was shown in Fig. 9(b). The induced voltage was weakest when the induction bar a was under the phase B (e.g., x=0), since the voltage induced by balanced three-phase overhead transmission lines mutually offset. The sensitivity was enhanced when the horizontal displacement of induction bars increased, i.e., approaching the horizontal displacement of phase C of overhead transmission lines. When the horizontal displacement of induction bars increased, the contribution from phase A of overhead transmission lines gradually decreased. The major sources were the phase B and C of overhead transmission lines, enabling the induced voltages larger. The largest sensitivity for three induction bars were attained when their horizontal displacement were about in the middle of phase B and C of overhead transmission lines. If the induction bars exceeded the horizontal displacement of phase C of the overhead transmission lines, the major contribution was only phase C. The induced voltages decreased when they were moved away since the induction bars were less coupled with the overhead transmission lines. Therefore, it is suggested to enable the

induction bars' horizontal displacement in the middle of adjacent phases of overhead transmission lines (phase A & phase B, or phase B & phase C) approximately for achieving a large sensitivity.

2) Spacing distance: the induced voltages of induction bars were calculated by adjusting the spacing distance between induction bars while fixing the altitudes, and the position of induction bar a. The induction bar a was located under the phase B of overhead transmission lines with 1 m altitude, and bar b and c were spaced with various distances in the simulation (d was set from 0 to 80 m). The sensitivity for three induction bars under various spacing distance was shown in Fig. 9(c). The sensitivity for induction bars b and c were enhanced when the spacing distances increased, as their horizontal displacement were changed at the same time. By looking into induced voltage of induction bar a as an example without horizontal displacement, the sensitivity would increase when the spacing distance became larger. Based on Eq. (8), the induced voltage of an induction bar a is calculated as

$$V_a \approx \lim_{Z_{a0}'' \to \infty} \sum_{i=A,B,C} \frac{Z_{a0} \cdot Z_{a0}''}{Z_{a0} Z_{a0}'' + Z_{ia} \left(Z_{a0} + Z_{a0}'' \right)} V_i$$
$$= \sum_{i=A,B,C} \frac{Z_{a0}}{Z_{a0} + Z_{ia} + \frac{Z_{ia} Z_{a0}}{Z_{a0}''}} V_i \qquad (11)$$

where V_i is the voltage of three-phase overhead transmission lines, and the equivalent impedances of respective capacitance are shown in the Fig. 3. By fixing the position of the induction bar a and meanwhile increasing the spacing distance between the induction bars (induction bar a & b, induction bar b & c), the capacitance between the induction bars decreases (i.e., C_{a0}'' in this case). As such, the equivalent impedance Z_{a0}'' increases accordingly, leading to the enhanced induced voltage of V_a according to Eq. (11). When the spacing distance further increases, the impedance Z_{a0}'' increases to a larger value. Therefore, the induced voltage of induction bar a is calculated as

$$V_a \approx \sum_{i=A,B,C} \frac{Z_{a0} \cdot Z_{a0}''}{Z_{a0} Z_{a0}'' + Z_{ia} \left(Z_{a0} + Z_{a0}'' \right)} V_i$$
$$= \sum_{i=A,B,C} \frac{Z_{a0}}{Z_{a0} + Z_{ia}} V_i \qquad (12)$$

where Z_{a0} is the impedance between induction bar a and the ground, and Z_{ia} ($i = A, B, C$) is the impedance between overhead transmission lines and induction bar a. As such, the induced voltage of induction bar a reaches an upper limit when the bar spacing increases. The calculation result of the induced voltage of the induction bar a is shown in Fig. 9(c), which is consistent with the above analysis. Though the sensitivity can be enhanced by increasing the bar spacing, the spacing distance should be optimized considering the sensor size.

3) Altitude: the induced voltages of induction bars were calculated by varying the altitude while fixing horizontal displacement and spacing distance. The induction bar a was located under phase B of the overhead transmission lines with 2 m spacing distances between induction bars, and

their altitudes were increased simultaneously in the simulation (*h* was set from 1 to 15 m). The sensitivity for three induction bars under various horizontal displacement was shown in Fig. 9(d). The sensitivity of induction bars were enhanced when the altitudes of induction bars increased, since the coupling between overhead transmission lines and induction bars became stronger. The sensitivity of three phases does not grow at the same rate since the electrical field distribution is not uniform. In this setup, the strongest electrical field is around the phase conductors of the overhead transmission lines. Since bar *a* is closest to the phase B of transmission lines among the three phases, larger voltage is induced on bar *a* when its altitude becomes higher (i.e., closer to phase B).

From the above analysis, the sensitivity of induction bars can be optimized by enabling the induction bars' horizontal displacement in the middle of adjacent phases of overhead transmission lines (phase A & phase B, or phase B & phase C) approximately. There should be a balance to enhance the sensitivity by increasing the spacing distances as the whole sensor system cannot get too large. Similarly, to increase the altitude of induction bars can increase the sensitivity while the altitude should be acceptable for platform installation and manipulation in practice.

E. Transient Over-Votlage Measurement

The established technique should be able to monitor the steady operation state of overhead transmission lines, and as well as, to monitor their transient over-voltages. Transient over-voltages occur in transmission lines such as by short circuit due to conductor clashing/grounding, or switching in the system for energizing transmission lines [32]. In short-circuit faults, the over-voltages are generally 1-2 p.u., and the frequency ranges from kHz to MHz [33]–[35]. The switching surges are about 1-3 p.u., and have high frequency up to kHz [36], [37]. The maximum 3 p.u. over-voltages of overhead transmission lines are attenuated by capacitive coupling, and thus still within the measurement range of the voltage sensor. Regarding the frequency response of the induction bars, their cut-off frequency response of capacitive coupling is calculated as

$$f = \frac{1}{2\pi\sqrt{LC}} \qquad (13)$$

where *L* and *C* are the mutual inductance and capacitance between overhead transmission lines and induction bars [38]. The capacitance and inductance between overhead transmission lines and induction bars are calculated as [39], [40]

$$C = \frac{\pi\varepsilon l}{ln(\frac{d}{a} + \sqrt{\frac{d^2}{a^2} - 1})} \qquad (14)$$

$$L \approx \frac{\mu_r}{\pi}cosh^{-1}\left(\frac{d}{a}\right)l \qquad (15)$$

where *l* is the overlapping length between the overhead transmission lines and the induction bars (i.e., the length of induction bars since they are shorter than transmission lines), *a* is induction bar radius and *d* is the distance between them. Since the typical height of transmission lines are from
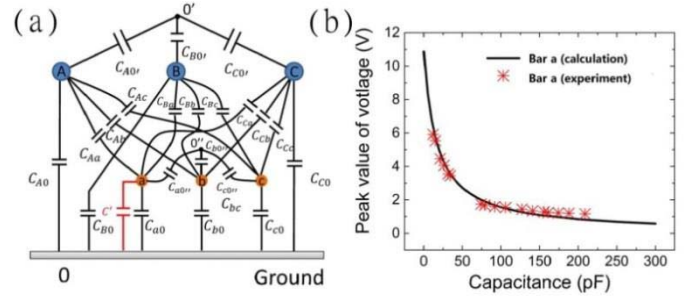

Fig. 10. Effect on induced voltage by additional capacitance of measuring instrument. (a) Additional capacitance (C') introduced by instrument. (b) Peak value of induced voltage on bar *a* as a function of the additional capacitance C'.

15 to 55 m [41], the designed platform can be around 1 to 2 meter above the ground, and thus the distance between them is tens of meters in reality. The radius of induction bars is in the order of mm, and the length of induction bars is only around a meter. Therefore, the inductance and capacitance between overhead transmission lines and induction bars are calculated in the order of μH and pF, respectively. As such, the frequency bandwidth for the sensor is calculated to be as high as MHz. The sensor established on the principle should be able to measure the high-frequency transient over-voltages status.

F. Effect of Measuring Equipment

The induced voltage on induction bars can then be measured by an instrument such as a voltage sensor or an oscilloscope. However, the intrinsic capacitor of the instrument is a major concern. For example, an oscilloscope can be treated as a large resistance (about MΩ) in parallel with an intrinsic capacitor. If the oscilloscope is used to measure the induced voltage of bar *a*, an additional capacitor needs to be introduced (C' in Fig. 10(a)) apart from the self-capacitance of bar *a*. From the circuit analysis in Fig. 10(a) and Eq. (9), the induced voltage of the bar *a* decreases as the additional capacitance increases because the total capacitance between bar *a* and ground becomes larger. The peak value of the induced voltage on bar *a* is calculated as a function of the additional capacitance C' and shown in Fig. 10(b).

Experiments were conducted with the scaled testbed in our laboratory to study the influence of such additional capacitance. The altitude of the three-phase overhead transmission lines (6 mm^2 PVC cable [42]) and induction bars were 0.50 and 0.20 m, and their conductor radii were 1.38 and 3 mm respectively. The spatial distances between adjacent conductors of overhead transmission lines (induction bars) were 0.16 m (0.32 m), and the horizontal distance (*x* in Fig.1) was 0.21 m. The three-phase overhead transmission lines were operating under 220 V 50 Hz AC mains voltage. The oscilloscope TEKTRONIX TDS 340 was used to measure the induced voltage on the induction bars. The voltage waveform induced on bar *a* was found almost to be sinusoidal with around 50 Hz frequency, and the induced peak voltage was measured to be 2.4 V. This result differs from the calculated
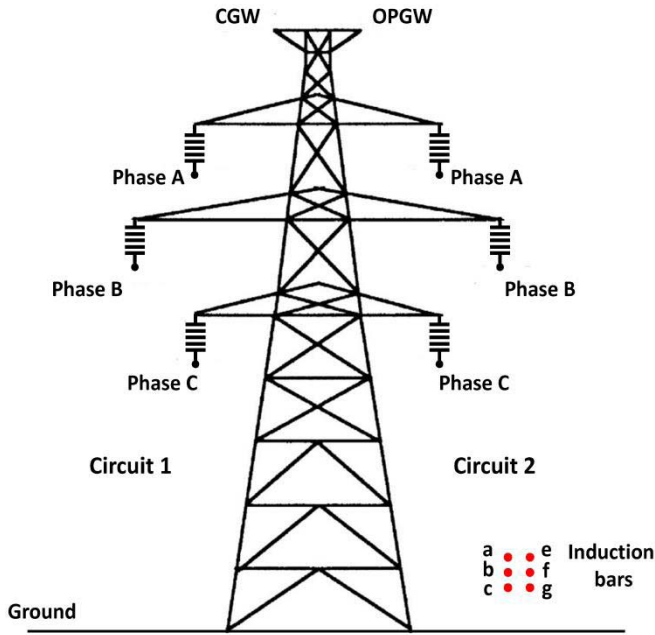
Fig. 11. Configuration of double-circuit transmission lines and induction bars.

induced voltage (10.872 V) by Eq. (9) without considering any additional capacitance. Such discrepancy is attributed to the additional capacitance introduced by the oscilloscope, which is determined to be around 59 pF by referring to the calculated curve in Fig. 10(b). In order to experimentally verify the relation between induced voltage and additional capacitance introduced by the instrument, extra capacitors were installed in series and in parallel to form various additional capacitance values in our setup. The resulting induced voltage on bar *a* was measured as plotted in Fig. 10(b). The measurement result matched with the calculated values well, indicating the analysis of additional capacitance is correct.

G. Multi-Circuit Extension

Multi-circuit transmission lines (e.g., double-circuit, quadruple-circuit, etc.) are also commonly deployed in power system for delivering more power over a particular distance with less cost for constructing extra transmission towers [29]. The sensor platform for multi-circuit transmission lines can be derived from the technique introduced for the single-circuit transmission lines in this paper accordingly.

For multi-circuit transmission lines, the phase voltages can be reconstructed by applying the same number of induction bars as the total phases of multi-circuit transmission lines to form a similar equation as Eq. (9). This is because the same number of linear equations are needed to solve all the unknowns (i.e., voltages of multi-circuit transmission lines). An example of a double-circuit transmission line for illustration is given in Fig. 11. The double-circuit transmission carries two independent three-phase circuits (i.e., 6 transmission lines in total), and correspondingly 6 induction bars are located on the ground level. Based on this setup, the coupled voltage of
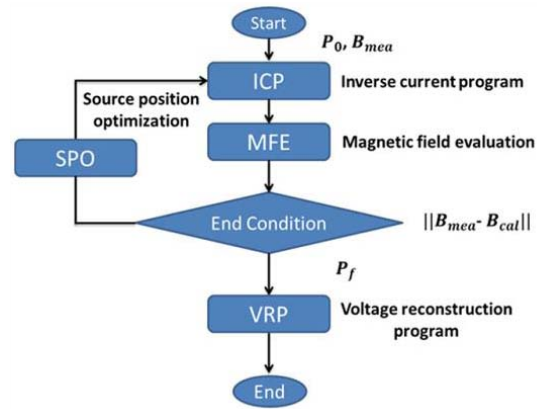

Fig. 12. Flowchart of real-time voltage-monitoring technique.

transmission lines and induction bars are related by

$$
\begin{bmatrix} V_a \\ V_b \\ V_c \\ V_e \\ V_f \\ V_g \end{bmatrix} = [Z]_{6\times6} \begin{bmatrix} V_{A1} \\ V_{B1} \\ V_{C1} \\ V_{A2} \\ V_{B2} \\ V_{C2} \end{bmatrix} \quad (16)
$$

where $V_{Ai}, V_{Bi}, V_{Ci}(i = 1, 2)$ are three-phase voltages of circuit 1 and 2, and $V_a, V_b, V_c, V_d, V_e, V_f$ are induced voltage of induction bars. The coefficient matrix (Z) now becomes 6×6 since each of the six transmission lines induces voltage on an induction bar, and there are six induction bars in total. The process to establish the matrix (Z) consists of the following steps (similar to the procedure for the single-circuit transmission line as introduced in the paper): (1) model the equivalent capacitors among six transmission lines, six induction bars and the ground; (2) calculate their capacitances according to their relative positions; (3) establish the equivalent electrical circuit for getting each coefficient of the matrix. Based on the induced voltage measurement, the phase voltage of each transmission line can be then reconstructed by Eq. (16). For other types of multi-circuit transmission lines, the process is similar. For example, 12 induction bars would be installed for establishing a similar equation to the Eq. (16) for the quadruple-circuit transmission lines, and this time it will be 12×12 coefficient matrix and there are 12 unknowns to solve. The position of induction bars can be arbitrary but it is better to keep the sensors small and located on the ground level for installation convenience. One criteria to note is that the induction bars cannot be located where their spatial relations to each phase of transmission lines are symmetrically the same to avoid having identical equations; otherwise, there would be insufficient number of equations to solve all the unknowns.

III. SENSING TECHNIQUE AND PLATFORM

A. Flowchart of Sensing Technique

The flowchart of this real-time voltage-monitoring technique for three-phase overhead transmission lines are shown in Fig. 12.
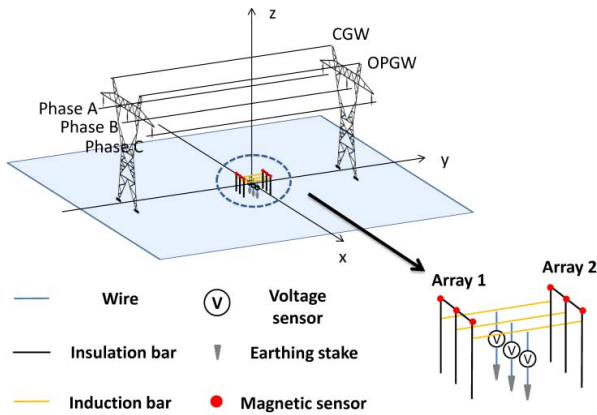
Fig. 13. Overview of three-phase transmission lines and sensing platform.

Stochastic optimization algorithm is adopted to process the measured magnetic field information. The inverse problem is daunting as spatial positions of three-phase conductors and loading currents are unknown and impossible to be solved analytically. The end condition of the algorithm is to minimize the Euclidian distance between measured and calculated magnetic signals. This part is depicted by the loop in Fig. 12, which consists of three modules, namely inverse current program (ICP), magnetic field evaluation (MFE) and source position optimization (SPO) [19]. The ICP algorithm starts with an initial cable position P_0 and measured magnetic field B_{mea} to determine the current value by least square method ($I = (A^T A)^{-1} A^T B_{mea}$) in which A is a coefficient matrix depending on source geometry. Then the MFE calculates the magnetic field B_{cal} by electromagnetic theory. If the Euclidian distance between B_{cal} and B_{mea} is smaller than the pre-set threshold, the algorithm terminates; otherwise, the cable position is updated by SPO which adopts genetic algorithm, and the iteration continues until the pre-set threshold is satisfied to output the final cable positions (P_f). Further details of this part can be found in [19]. Based on the relative positions between overhead transmission line and induction bars, the capacitance of capacitive coupling between overhead transmission lines and induction bars are acquired. The equivalent electric circuit model can be then established and analyzed, and the coupled voltage transformation matrix to correlate voltage of overhead transmission lines and induction bars mathematically is formed in the voltage reconstruction program (VRP).

B. Platform Design for Voltage Monitoring

Transmission towers uphold high-voltage (*e.g.,* 10, 35, 110, 220 or 500 kV) transmission conductors. A section of three-phase overhead transmission lines are supported by the lattice towers as shown in Fig. 13. Since magnetic-field sensing is integrated to restore conductor positions of three-phase overhead transmission lines, magnetic sensors are assembled together with induction bars on the ground. The induction bars are oriented along the direction of the overhead transmission lines. The overview of the platform is shown in Fig. 13, and the details of its components are introduced as follows:

(i) Induction bars: three horizontally parallel induction bars are upheld along the direction of the transmission lines by upright insulation bars (*e.g.*, polymethyl methacrylate) at both ends. The induction bars must be electrically conductive and non-magnetic so that the magnetic signals emanated from the transmission lines would not be altered. Copper can be a low-cost candidate material. The length of induction bars cannot be too short as the capacitance calculation can be distorted by fringe effects of the conductors in reality.

(ii) Magnetic sensors: in order to acquire relative positions between overhead transmission line and induction bars, an array of magnetic sensors is installed at each end of the induction bars. The relative positions between magnetic sensors and induction bars can be arbitrary, and in our case they are installed right above the induction bars for illustration. Also, they are at the same altitude and evenly distributed horizontally. The number of magnetic sensors can affect the accuracy of restored conductor position results [19]. More magnetic sensors can provide more data for the stochastic optimization algorithm and thus improve the reconstruction accuracy. Through measuring the magnetic field by array 1 and 2, the spatial position of overhead transmission lines can be determined respectively. Then the direction of overhead transmission lines can be derived. In practice, these magnetic sensors can be implemented by magnetoresistive sensors which are compact in size and low cost. The frequency response of MR sensors are up to MHz [43] and they are able to tackle high-frequency signals.

IV. SIMULATION VALIDATION

The sensing technique was tested both in normal and faulty conditions respectively by simulation on three-phase high-voltage overhead transmission lines. The real measured signals were simulated with noises as in the real world. The magnetic signals can be contaminated by intrinsic noise of magnetic sensors together with background interferences. The non-ideality of magnetic sensors can be offset error, hysteresis error, and various sources of noise in sensor. Some of these influences can be eliminated while some cannot. For example, offset drift due to temperature variation in a magnetic sensor can be canceled by a temperature compensation circuit [44]. However, hysteresis error and various intrinsic sources of noise cannot be totally removed. Taking the off-the-shelf magnetic sensor, Honeywell HMC2003, as an example, its hysteresis error can be strong as 100 nT [43]. Among thermal noise, $1/f$ noise and shot noise in magnetic sensors, the $1/f$ noise is the main limitation of performance at 50 Hz. A summary of noise level for popular magnetic sensors with preamplifiers at room temperature is given in [45]. The maximum $1/f$ noise level at low frequency for these magnetic sensors is typically 10 nT. The noise induced by atmospheric electromagnetic activity is generally to be 10 nT [46]. These noises are uncorrelated random and thus the white noise type is adopted. As such, a total mean value of 120 nT white noise was simulated to contaminate the magnetic signals emanated from overhead transmission lines, consisting of assumed 10 nT external environment effect, 100 nT intrinsic error and
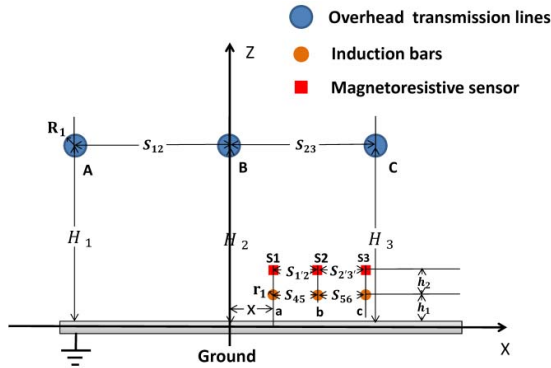
Fig. 14. Layout of three-phase overhead transmission lines, induction bars, magnetoresistive sensors and ground in simulation. The altitude of overhead transmission lines (induction bars) are H_1, H_2, and H_3 (h_1, h_2, and h_3). The spatial between overhead transmission lines (induction bars) is S_{12} and S_{23} (S_{45} and S_{56}). The radius of overhead transmission line (induction bar) is R_1 (r_1). The magnetoresistive sensors (S_1, S_2 and S_3) are above induction bars with h_2 altitude, and their spatial distances are $S_{1'2'}$ and $S_{2'3'}$.

10 nT $1/f$ noise. The induced voltage signals on induction bars were also contaminated. In the case it is assumed that there only exist the overhead transmission lines in the space, and thus the induced voltages on the induction bars are pure. The signals, however, can be affected by the data transmission and acquisition system. We accordingly simulated a case of a medium-quality measurement system with signal-to-noise ratio of 40 dB [47].

The configuration for three-phase overhead transmission lines, induction bars, and magnetic sensors is depicted in Fig. 14. The 10 kV three-phase overhead-transmission-line (5773.5 V phase voltage) model was simulated with 50 Hz and 1000 A phase current. The altitude of the three-phase conductors (H_1, H_2, and H_3) were 20 m, and the spatial distance of them (S_{12} and S_{23}) was 10 m. The radii of overhead transmission lines (R_1) were 0.015 m. The altitude of the induction bars (h_1) were 1 m and their radii (r_1) were 0.010 m. The spatial distance of induction bars (S_{45} and S_{56}) and magnetic sensors ($S_{1'2'}$ and $S_{2'3'}$) were both 2 m while the magnetic sensors were 0.5 m (h_2) above the induction bars. The horizontal distance (x) between phase B (transmission line) and bar a (induction bar) was 2 m. In the simulation, the induction bars were strictly aligned along the direction of the overhead transmission lines.

A. Normal Condition

The magnetic sensors (denoted by S1, S2 and S3 in Fig. 14) recorded real-time magnetic field with sampling rate of 20 kHz. The normal signal and noisy signals measured by the magnetic sensor S1 in the X-axis are shown in Fig. 15(a). The reconstructed phase conductor positions in both normal and noisy conditions are depicted in Fig. 15(b). The average reconstructed positions based on the noisy signals were phase A (-10.03, 20.07), phase B (0.26, 19.88), and phase C (9.88, 20.18), which were deviated from the real positions of phase A (-10.00, 20.00), phase B (0, 20.00), and phase C (10.00, 20.00) with large errors. The same situation can be found in the voltage reconstruction process. The noisy induced
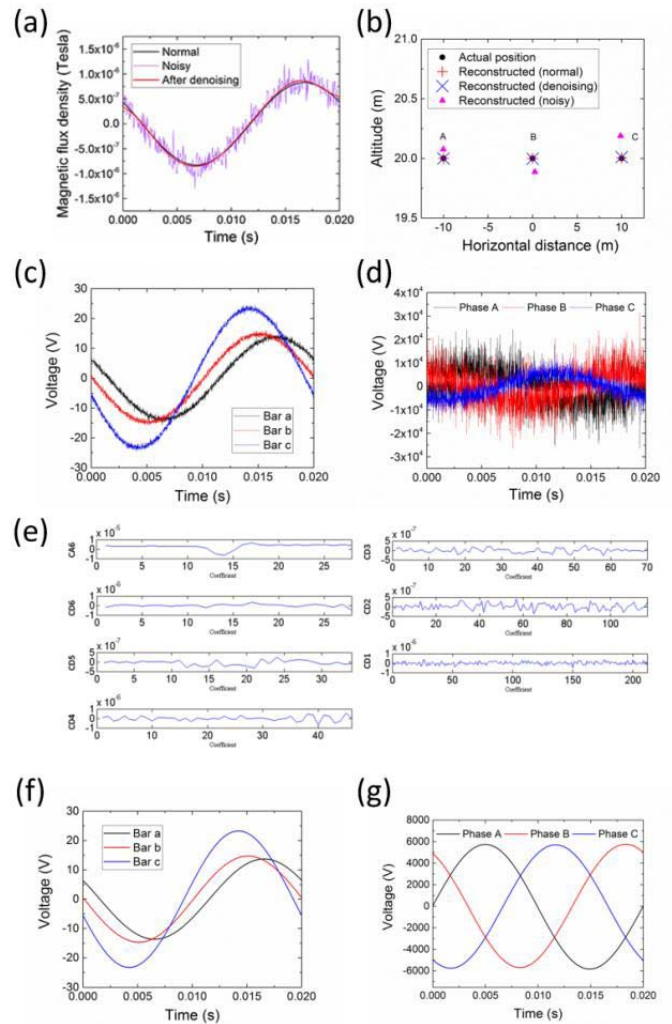

Fig. 15. Measured signals and reconstruction results in normal condition. (a) Normal, noisy, and de-noised magnetic signal of one cycle in X-axis measured by magnetic sensor S1. (b) Position reconstruction from normal, noisy and de-noised magnetic signals. (c) Noisy induced voltage signals of induction bars. (d) Voltage of overhead transmission line reconstructed from noisy voltage signals of induction bars. (e) Wavelet coefficients for X-axis of magnetic sensor S1. (f) Induced voltages of induction bars after de-noising. (g) Voltage of overhead transmission lines reconstructed from the de-noised induced voltages of induction bars.

voltage of induction bars are shown in Fig. 15(c), and the reconstructed results of the overhead transmission lines are of bad quality as shown in Fig. 15(d).

In order to improve the reconstruction results, wavelet-based de-noising algorithm was applied. The procedure of wavelet de-noising is composed of three steps: (1) apply wavelet transform by mother wavelet to the noisy signals to generate wavelet coefficients in a certain level which can properly distinguish signals; (2) select appropriate threshold limit and threshold method to remove the noises; (3) inverse wavelet transform to obtain a de-noised signal. By setting a level of decomposition, it enables to analyze the signal in various frequency bands and results in corresponding wavelet coefficients. Universal thresholding is performed to set zeros for all wavelet coefficients with absolute value smaller than

the preset threshold value in this case [48], [49], which is calculated as

$$\lambda = \frac{MAD}{0.6745}\sqrt{2\log(n)} \tag{17}$$

where *MAD* is the mean absolute deviation of all wavelet coefficients, and *n* is sample size [50]. In the simulation, the Symlets wavelet (i.e., sym12) was adopted, and the decomposition level to de-noise contaminated signal was set as 6. The wavelet coefficients for each bandwidth (CA6: 0-312.5 Hz; CD6: 312.5-625 Hz; CD5: 625-1250 Hz; CD4: 1250-2500 Hz; CD3: 2500-5000 Hz; CD2: 5000-10000 Hz; CD1: 10-20 kHz;) are shown in Fig. 14(e). The de-noised magnetic signals in the X-axis of magnetic sensor S1 are shown in Fig. 15(a) again, and they closely resemble the normal signal. The average reconstructed cable positions calculated by de-noised signals match the real physical configuration as depicted in Fig. 15(b). The same process was taken to de-noise the noisy induced voltage signals and the results are depicted in Fig. 15(f). Based on the de-noised signals, the reconstructed voltage of overhead transmission lines are shown in Fig. 15(g). The voltage peaks of phase A, B and C are 5743.19, 5762.36 and 5707.20 V with error of 0.52%, 0.19% and 1.14% respectively, as compared to the rated value of 5773.5 V. The voltage trough of phase A, B and C are −5830.18, −5692.53 and −5750.44 V with error 0.95%, 1.40% and 0.39% respectively, as compared to the rated value of 5773.5 V. The reconstructed frequency for phase A, B and C are 50.40, 49.75 and 50.15 Hz with error 0.80%, 0.49% and 0.30% respectively. As such, the technique demonstrates to reconstruct the voltage status with merely small error in normal condition.

B. Transient Over-Voltages

A variety of transient faults can happen in a power system. A single-phase earth fault in the isolated neutral system is simulated based on [51] which describes a single-phase arc ground on the busbar of a 10 kV three-phase overhead transmission network in Xueying substation of China. Phase A encountered single-phase arcing-ground short circuit fault and voltages were measured on the transmission line. The voltage variations of three-phase overhead transmission lines are depicted in Fig. 16(a). The voltage of phase A was modeled as an attenuating sinusoidal curve. Its initial amplitude, damping factor, frequency were 5773.5 V, 1000 and 10 kHz, respectively. Voltage of phase A dropped to zero after several seconds while phase B and C continued with $\sqrt{3}$ times amplitude amplification (compared to the rated value of 5773.5 V) and changed to 150° phase differences after the transient fault. The sampling rate in the simulation was set to be 30 kHz. The noisy induced voltage signals on the induction bars are shown in Fig. 16(b). Wavelet transform was conducted with decomposition level of 10 again. In the case the main frequency bandwidth (50 Hz and 10 kHz) were retained, as shown in Fig. 16(c) by frequency spectrum analysis. The reconstructed voltages of overhead transmission lines are shown in Fig. 16(d), where the high-frequency conditions can be recognized in the early state. The reconstructed voltages are consistent with the voltages signals in Fig. 16(a).
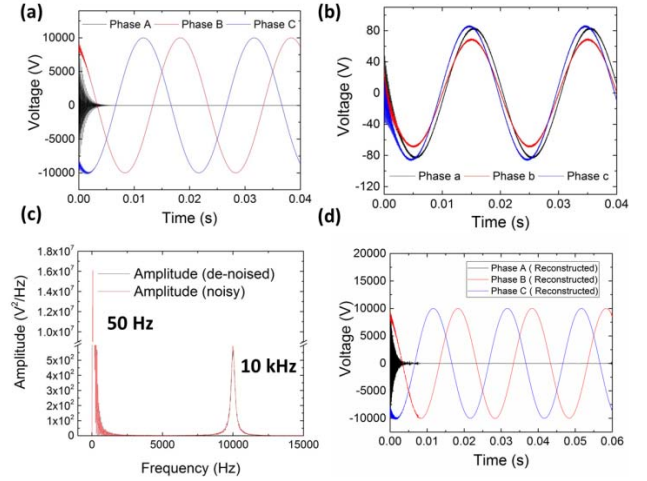

Fig. 16. Voltage of overhead transmission line and frequency analysis in faulty condition. (a) Voltage of overhead transmission line in transient fault of single-phase arcing-ground short circuit in phase A. (b) Noisy signals of induction bars. (c) Frequency analysis of the induced voltage of induction bar *a*. (d) Voltage of overhead transmission lines reconstructed from the de-noised induced voltages of induction bars.

As such, the technique demonstrates to reconstruct the voltage information successfully in faulty condition.

V. EXPERIMENTAL VALIDATION AND DISCUSSION

A. Normal Condition

The scaled testbed in the lab was established to validate the technique, as shown in Fig. 17. The three-phase overhead transmission lines were operating under 220 V 50 Hz AC mains voltage. The altitude of the overhead transmission lines (6 mm^2 PVC cable [42]) was 0.50 m and spaced by 0.16 m distance between two adjacent phases. The induction bars were made of copper, and their altitude and length were 0.04 and 1.5 m, respectively. The induction bars were of 3 mm radius and spaced by the distance of 0.06 m. Magnetic sensors (HMC2003, Honeywell) were installed 0.08 m above the induction bars. The horizontal distance between phase B (overhead transmission line) and bar a (induction bar) was 0.08 m. The permalloy-based Honeywell HMC2003 is an integrated sensor system capable of measuring magnetic fields generated by overhead transmission lines in a plane by two mutually orthogonal sensing axes. These compact-in-size sensors (19×25.4 mm^2) were operated under 12 V DC power supply. The aluminum board was paved as the ground and connected to the ground wire of the building to ensure its zero electric potential. The sensor array 1 and 2 were established 10 cm away from respective end of induction bars.

The magnetic signals of sensors in a cycle were acquired and de-noised, and their RMS values were processed to reconstruct the spatial positions of overhead transmission lines. The actual and reconstructed positions of overhead transmission lines are shown in Fig. 18. The reconstructed position of each phase is very close to the actual configuration with error less than 1 cm as shown in Table I. In the testbed, the overhead transmission lines were straightened without sagging. The position values of each transmission line are reconstructed
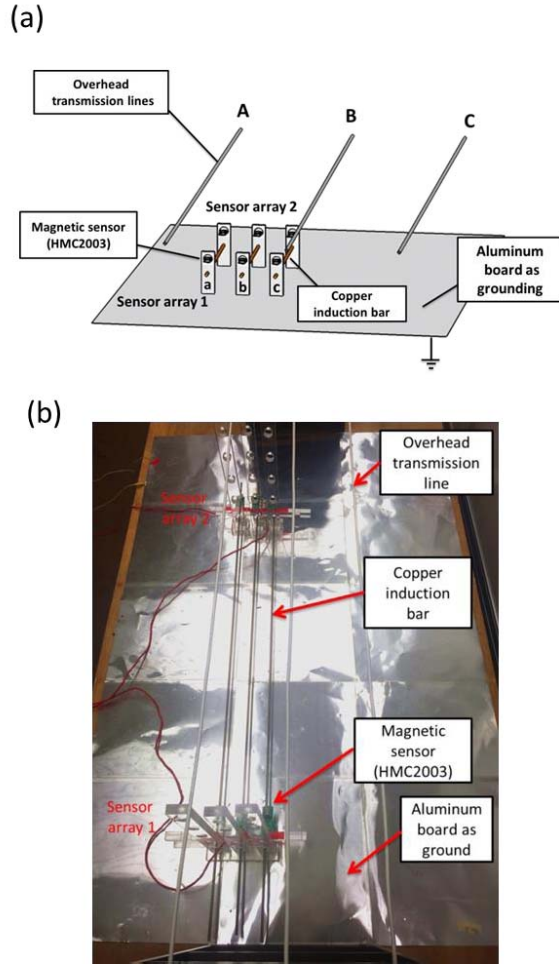
Fig. 17.   Scaled testbed to test and validate the proposed technique for monitoring voltage, comprised of three-phase overhead transmission lines, magnetic sensors (HMC2003), copper induction bars, and aluminum board as grounding. (a) Schematic diagram. (b) Image of scaled testbed established in the lab.
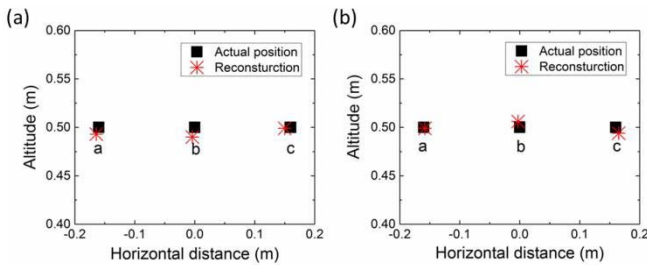

Fig. 18.   Reconstructed phase positions of overhead transmission lines. (a) Spatial positions reconstructed from array 1. (b) Spatial position reconstructed from array 2. Actual position of overhead transmission lines are obtained by averaging these two reconstruction results.

from the data of the array 1 and 2, and then averaged to be adopted as the actual spatial position of that line for further processing, namely A $(-0.161, 0.496)$, B $(0.003, 0.498)$, and C $(0.161, 0.496)$ (units in m).

The induced voltages of induction bars were measured by the oscilloscope TEKTRONIX TDS 340 with 100 kHz sampling rate. The noisy induced voltages in a time cycle is

TABLE I

ACTUAL AND RECONSTRUCTED POSITIONS OF
OVERHEAD TRANSMISSION LINES

Position		Phase a (x, y) (m)	Phase b (x, y) (m)	Phase c (x, y) (m)
Array 1	Reconstructed	(-0.164, 0.493)	(-0.0041, 0.49)	(0.158, 0.499)
	Actual	(-0.160, 0.500)	(0, 0.500)	(0.160, 0.500)
	Error	(0.004, 0.007)	(0.0041, 0.01)	(0.002, 0.001)
Array 2	Reconstructed	(-0.158, 0.499)	(-0.0028, 0.506)	(0.165, 0.494)
	Actual	(-0.160, 0.500)	(0, 0.500)	(0.160, 0.500)
	Error	(0.002, 0.001)	(0.0028, 0.006)	(0.005, 0.006)

shown in Fig. 19(a), and its Fourier transform is expressed in Fig. 19(b) by taking bar a as an example. In order to de-noise the measured signals, the wavelet de-noising algorithm was applied again. The decomposition level was set to 9, and the wavelet coefficients for each bandwidth (CA9: 0-195.3 Hz; CD9: 195.3-390 Hz; CD8: 390-781 Hz; CD7: 781.2-1565.5 Hz; CD6: 1562.5-3125 Hz; CD5: 3125-6250 Hz; CD4: 6250-12500 Hz; CD3: 12.5-25 kHz; CD2: 25-50 kHz; CD1: 50-100 kHz) are shown in Fig. 19(c). The universal threshold is calculated as 0.9617, and the main coefficients in CA9 were retained. The wavelet coefficients smaller than the threshold are removed, and the voltage waveforms of induction bars after de-noising are shown in Fig. 19(d). The frequency for the de-noised induced voltages mainly is 50 Hz as expressed in Fig. 19(e) by Fourier transform. The real voltage on each phase of overhead transmission line was measured in order to compare with the reconstructed result. The electric wiring diagram is shown in Fig. 19(f). A differential probe (GE8115, Elditest) was used for safe measurement of the high voltage. The differential probe clamped the live (L) and ground (G) wires for each phase. The probe can bear max 1500 V input voltage and the input voltage can be stepped down by a factor of 100. Then voltage waveform can be displayed on the oscilloscope. Based on the reconstructed configuration of the overhead transmission lines, the relative positions of overhead transmission lines and induction bars can be attained. Through establishing equivalent electric circuit model for capacitive coupling between overhead transmission lines and induction bars, the coupled voltage transformation matrix was successfully formed to correlate voltage of overhead transmission lines with induced voltage of induction bars so that the voltages of the overhead transmission lines can be reconstructed. The reconstructed and measured voltages of overhead transmission lines are shown in Fig. 19(g). As shown in Table II, the reconstructed voltage peaks of phase A, B and C are 306, 313 and 305 V, and the troughs are -305.6, -309.2 and -320.5 V respectively. The measured voltage peaks of phase A, B and C are 300, 308 and 300 V, and the troughs are -316, -324 and -316 V respectively. The maximum relative between the measured and reconstructed were
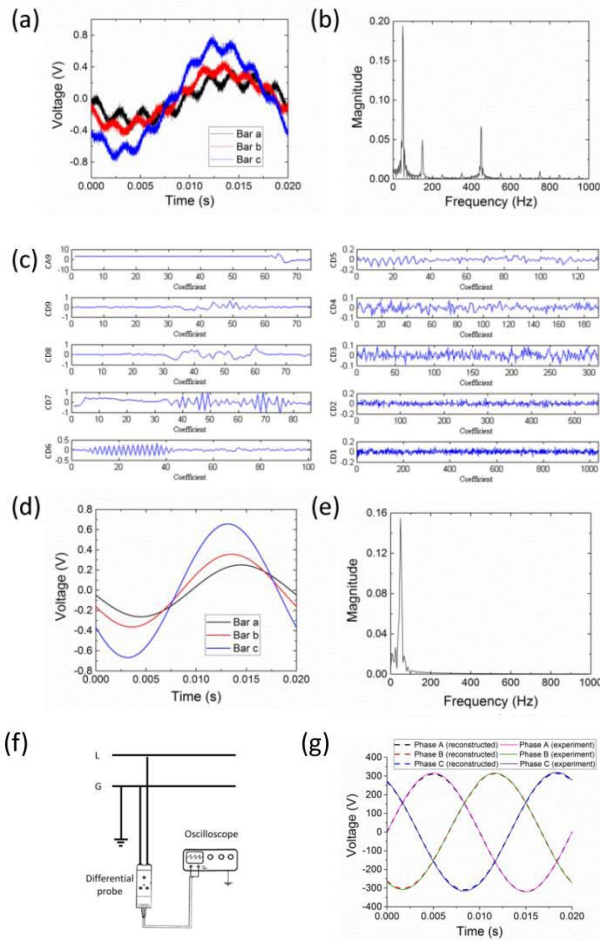
Fig. 19. Measured voltage and reconstruction results with testbed. (a) Voltage measured from induction bars. (b) Frequency analysis for induction bar *a*. (c) Wavelet coefficients for analyzing induced voltage of induction bar *a*. (d) Waveform of the induced voltage after de-noising. (e) Frequency analysis for induction bar *a* after de-noising. (f) Voltage measurement by differential probe clamped between live (L) and ground (G). (g) Comparison between reconstructed and actual measurement voltage of overhead transmission lines.

TABLE II
COMPARISON BETWEEN RECONSTRUCTED AND ACTUAL MEASUREMENT
VOLTAGE OF OVERHEAD TRANSMISSION LINES

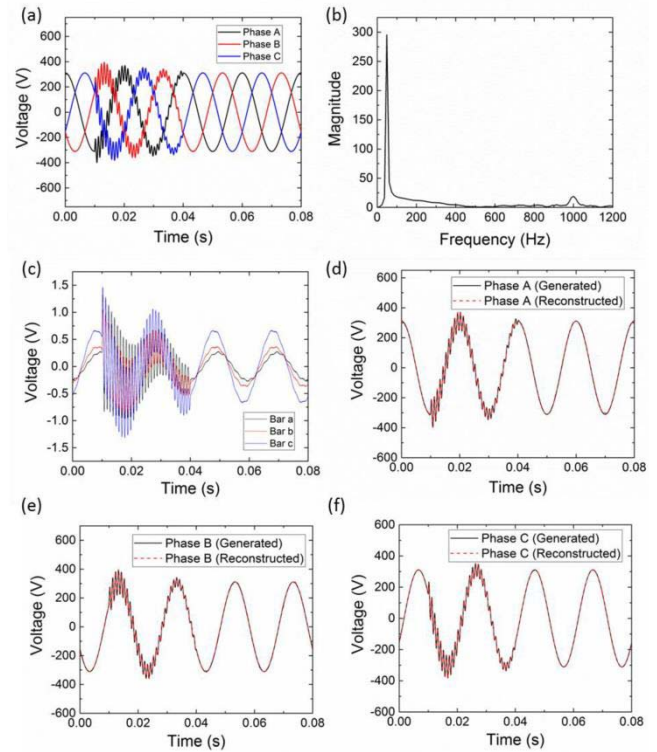| Phase	Peak			Trough		
	Reconstructed (V)	Measured (V)	Relative error	Reconstructed (V)	Measured (V)	Relative error
A	306	**300**	**2 %**	-305	**-316**	**3.5 %**
B	313	**308**	**1.6 %**	-309	**-324**	**1.5 %**
C	305	**300**	**1.6 %**	-320	**-316**	**1.3 %**

Fig. 20. Measured voltage and reconstruction results with testbed for switching over-voltages. (a) Voltage generated from AC source. (b) Frequency spectrum of generated waveform. (c) Voltage measured on induction bars. (d) Reconstructed versus generated voltage of Phase A. (e) Reconstructed versus generated voltage of Phase B. (f) Reconstructed versus generated voltage of Phase C.

3.5 % in trough value of phase A. The measured frequency of phase A, B and C are 50.7, 50.1 and 50.3 Hz, respectively. Compared with the reconstructed results (51.67, 50.5 and 49.5 Hz for phase A, B and C), the errors are 1.9 %, 0.8 % and 1.6 %, respectively. As such, the technique demonstrates to reconstruct the voltage status with merely small error in normal condition. These experimental results with the testbed demonstrate that the proposed technique is practical and feasible for monitoring voltage of overhead transmission lines.

B. Transient Over-Voltages

Apart from the fault case illustrated in Section IV.(b), switching transient over-voltages receive special attentions since it impacts the power quality [52]. Because a capacitor voltage cannot change instantaneously, an immediate voltage drop process followed by a fast voltage recovery gives a high-frequency oscillating transient voltages superimposed on the fundamental frequency. Typical over-voltage levels range from 1-2 p.u., and the frequency is up to kHz.

The experiment for high-frequency switching surges was conducted to validate the sensor ability for transient over-voltage monitoring, and the typical waveforms were generated by a programmable AC source (Chroma 61704). The surge case happens when the switching of capacitor banks are closed for reducing the magnitude of the reactive power drawn by the load from the utility distribution system. The setup of overhead transmission lines and induction bars were consistent with the normal condition test in Fig. 17. In the normal operation state, the capacitor banks were switched on at 0.01s and incurred an oscillation, decaying within one and a half cycle (Fig. 20(a)). The frequency spectrum denoted the signals had a high-frequency signal of 1 kHz (Fig. 20(b)). The induced voltages on induction bars were measured by the

oscilloscope TEKTRONIX TDS 340 with 100 kHz sampling rate as shown in Fig. 20(c). The wavelet de-noising was applied with Sym15 wavelet in the decomposition of level 4. The reconstructed voltages for three phases are shown in Fig. 20(d)-(f), and the high-frequency oscillation were successfully reconstructed. The reconstructed voltages matched well with the original waveforms in Fig. 20(a). Therefore, the platform was demonstrated to work successfully in transient over-voltage monitoring.

VI. CONCLUSION AND FUTURE WORKS

This work aims at developing a non-contact technique to monitor the voltage of overhead transmission line via capacitive coupling with the assistance of magnetic-field sensing. The technique was demonstrated on a single-circuit transmission line but the principle is also applicable for multi-circuit transmission lines. Through establishing equivalent electric circuit model for capacitive coupling between overhead transmission lines and induction bars, the coupled voltage transformation matrix was successfully formed to correlate voltage of overhead transmission lines with induced voltage of induction bars mathematically. The FEM simulation validated such voltage correlation. The study was also carried out to analyze the effect of ground wires, sensitivity of induction bars. Also, it was found that the additional capacitance introduced by the measuring instrument can affect the original equivalent electric circuit model, causing the induced voltage to drop significantly. This additional capacitance from the measuring instrument was taken into account in the equivalent circuit model for forming coupled voltage transformation matrix. By integration of magnetic-field sensing, the spatial positions of three-phase overhead transmission lines were acquired. The wavelet de-noising algorithm was supplemented to process the measured signals affected by noises. The technique was successfully demonstrated on a 10 kV three-phase overhead transmission network in simulation under normal and faulty conditions respectively. A scaled testbed was established in the lab to monitor the 220 V steady-state operating condition, and also the high-frequency transient over-voltages (a switching surge up to 1 kHz). The reconstructed voltages match well with the actual values, proving the feasibility and practicality of the proposed technique.

This voltage-monitoring technique can potentially offer advantages of higher measurement upper limit, wider frequency response and large-scale deployment for reliable operation, maintenance and development of overhead transmission grids. Since it is a non-contact technique, direct high-voltage measurement can be avoided. Through capacitive coupling, the induced voltages on induction bars are stepped down. Even facing with serious overvoltage in faulty incident of overhead transmission lines, the induced voltages on induction bars are still within the measurement range. This in a way broadens the voltage range that we can measure from the overhead transmission lines. The frequency bandwidth is also improved to MHz as compared to kHz range of the traditional PT approach. The enhanced voltage sensing ability in terms of magnitude and frequency can greatly facilitate identification of transient faults in overhead high-voltage transmission

lines. The compact size, reduced cost, and the non-galvanical connection (thus easy installation) enable the platform to be deployed in large scale to realize sectional monitoring and improve situational awareness.

The technique to monitor current of overhead transmission lines has already been achieved [19]. In the future, with the successful combination of these real-time voltage and current measurement techniques of overhead transmission lines, we can further develop a technique to monitor the power delivered by overhead transmission lines.

REFERENCES

[1] A. S. Al-Fuhaid and M. M. Saied, "A method for the computation of fault transients in transmission lines," *IEEE Trans. Power Del.*, vol. 3, no. 1, pp. 288–297, Jan. 1988.

[2] J. M. Carrasco *et al.*, "Power-electronic systems for the grid integration of renewable energy sources: A survey," *IEEE Trans. Ind. Electron.*, vol. 53, no. 4, pp. 1002–1016, Jun. 2006.

[3] J. A. Kumar, S. S. Venkata, and M. J. Damborg, "Adaptive transmission protection: Concepts and computational issues," *IEEE Trans. Power Del.*, vol. 4, no. 1, pp. 177–185, Jan. 1989.

[4] R. H. Bhuiyan, R. A. Dougal, and M. Ali, "A miniature energy harvesting device for wireless sensors in electric power system," *IEEE Sensors J.*, vol. 10, no. 7, pp. 1249–1258, Jul. 2010.

[5] N. M. Roscoe and M. D. Judd, "Harvesting energy from magnetic fields to power condition monitoring sensors," *IEEE Sensors J.*, vol. 13, no. 6, pp. 2263–2270, Jun. 2013.

[6] M. N. Alam, R. H. Bhuiyan, R. A. Dougal, and M. Ali, "Design and application of surface wave sensors for nonintrusive power line fault detection," *IEEE Sensors J.*, vol. 13, no. 1, pp. 339–347, Jan. 2013.

[7] D. Jovcic, N. Pahalawaththa, and M. Zavahir, "Analytical modelling of HVDC-HVAC systems," *IEEE Trans. Power Del.*, vol. 14, no. 2, pp. 506–511, Apr. 1999.

[8] M. Wang, A. J. Vandermaar, and K. D. Srivastava, "Improved detection of power transformer winding movement by extending the FRA high frequency range," *IEEE Trans. Power Del.*, vol. 20, no. 3, pp. 1930–1938, Jul. 2005.

[9] T. Imura, H. Okabe, T. Uchida, and Y. Hori, "Study of magnetic and electric coupling for contactless power transfer using equivalent circuits," *IEEE Ind. Appl. Mag.*, vol. 130, no. 1, pp. 84–92, Jan. 2010.

[10] T. Imura, H. Okabe, T. Uchida, and Y. Hori, "Wireless power transfer during displacement using electromagnetic coupling in resonance," *IEEE Trans. Ind. Appl.*, vol. 130, no. 1, pp. 76–83, Jan. 2010.

[11] G. E. Leyh and M. D. Kennan, "Efficient wireless transmission of power using resonators with coupled electric fields," presented at the 40th Power Symp., Calgary, AB, Canada, 2008.

[12] K. Wang, X. Qiu, S. Guo, and F. Qi, "Fault tolerance oriented sensors relay monitoring mechanism for overhead transmission line in smart grid," *IEEE Sensors J.*, vol. 15, no. 3, pp. 1982–1991, Mar. 2015.

[13] R. S. Nichols, "The first electric power transmission line in North America-Oregon City, Oregon," *IEEE Ind. Appl. Mag.*, vol. 9, no. 4, pp. 7–10, Jul. 2003.

[14] E. Culurciello and A. G. Andreou, "Capacitive inter-chip data and power transfer for 3-D VLSI," *IEEE Trans. Circuits Syst. II, Express Briefs*, vol. 53, no. 12, pp. 1348–1352, Dec. 2006.

[15] Y. Kami and W. Liu, "Analysis of coupling between transmission lines in arbitrary directions," presented at the IEEE Int. Symp. Electromagn. Compat., Denver, CO, USA, 1998.

[16] R. G. Olsen and K. C. Jaffa, "Electromagnetic coupling from power lines and magnetic field safety analysis," *IEEE Trans. Power App. Syst.*, vol. PAS-103, no. 12, pp. 3595–3607, Dec. 1984.

[17] Q. Chen, K. Ozawa, Q. Yuan, and K. Sawaya, "Antenna characterization for wireless power-transmission system using near-field coupling," *IEEE Antennas Propag. Mag.*, vol. 54, no. 4, pp. 108–116, Aug. 2012.

[18] C. P. Wang, D. H. Liu, and J. Jianguo, "Study of coupling effects among passive components used in power electronic devices," presented at the 4th Int. Power Electron. Motion Cont. Conf., Xi'an, China, Aug. 2004.

[19] X. Sun, Q. Huang, Y. Hou, L. Jiang, and P. W. T. Pong, "Noncontact operation-state monitoring technology based on magnetic-field sensing for overhead high-voltage transmission lines," *IEEE Trans. Power Del.*, vol. 28, no. 4, pp. 2145–2153, Oct. 2013.

[20] F. V. B. de Nazare and M. M. Werneck, "Hybrid optoelectronic sensor for current and temperature monitoring in overhead transmission lines," *IEEE Sensors J.*, vol. 12, no. 5, pp. 1193–1194, May 2012.

[21] K. Zhu, W. K. Lee, and P. W. T. Pong, "Non-contact electric-coupling-based and magnetic-field-sensing-assisted technique for monitoring voltage of overhead power transmission lines," presented at the IEEE Sensors Conf., Busan, South Korea, Nov. 2015.

[22] F. D. Şurianu, "Determination of the induced voltages by 220 kV electric overhead power lines working in parallel and narrow routes. Measurements on the ground and mathematical model," *WSEAS Trans. Power Syst.*, vol. 8, pp. 264–267, Aug. 2009.

[23] Wikipedia. (2012). *Overhead Power Line*, accessed on Aug. 29, 2016. [Online]. Available: https://en.wikipedia.org/wiki/Overhead_power_line#Ground_wires

[24] C. Furse, P. Smith, M. Safavi, and C. Lo, "Feasibility of spread spectrum sensors for location of arcs on live wires," *IEEE Sensors J.*, vol. 5, no. 6, pp. 1445–1450, Dec. 2005.

[25] Electrical Systems. (2011). *Transmission Tower Types*, accessed on Aug. 29, 2016. [Online]. Available: http://www.skm-eleksys.com/2011/02/transmission-tower-types.html

[26] T.-H. Chen and W.-C. Yang, "Analysis of multi-grounded four-wire distribution systems considering the neutral grounding," *IEEE Trans. Power Del.*, vol. 16, no. 4, pp. 710–717, Oct. 2001.

[27] S. Kurokawa, J. P. Filho, M. C. Tavares, C. M. Portela, and A. J. Prado, "Behavior of overhead transmission line parameters on the presence of ground wires," *IEEE Trans. Power Del.*, vol. 20, no. 2, pp. 1669–1676, Apr. 2005.

[28] J. Wang, Y. Wang, X. Peng, X. Li, X. Xu, and X. Mao, "Induced voltage of overhead ground wires in 500-kV single-circuit transmission lines," *IEEE Trans. Power Del.*, vol. 29, no. 3, pp. 1054–1062, Jun. 2014.

[29] H. Xiande and Z. Hao, "Simulation and analysis of induced voltage and induced current on overhead ground wire of Jindongnan-Nanyang-Jingmen 1000kV UHV AC transmission line," presented at the 4th Int. Conf. Elect. Utility Power Technol., Shandong, China, 2011.

[30] J. R. Vig and F. L. Walls, "A review of sensor sensitivity and stability," presented at the Int. Freq. Control Symp., Kansas City, MO, USA, Jun. 2000.

[31] A. D'Amico and C. Di Natale, "A contribution on some basic definitions of sensors properties," *IEEE Sensors J.*, vol. 1, no. 3, pp. 183–190, Oct. 2001.

[32] M. Patel and R. N. Patel, "Transient energy and its impact on transmission line faults," *Int. J. Eletrical. Comput. Energetic Electron. Eng.*, vol. 5, no. 8, pp. 1070–1076, 2011.

[33] M. A. Laughton and M. G. Say, *Electrical Engineer's Reference Book*. Amsterdam, The Netherlands: Elsevier, 2013.

[34] S. Hidiroğlu and M. U. Ünver. (2015). *Transient Analysis of Short-Circuit Faults Occuring in Cascade Connected Overhead Line/Cable Systems: Effect of Fault Type.* accessed on Sep. 30, 2016. [Online]. Available: http://www.emo.org.tr/ekler/83b65c888b720c9_ek.pdf

[35] J. C. Das, *Power System Analysis: Short-Circuit Load Flow and Harmonics*. Boca Raton, FL, USA: CRC Press, 2016.

[36] A. H. Soloot, A. Gholami, E. Agheb, A. Ghorbandaeipour, and P. Mokhtari, "Investigation of transmission line overvoltages and their deduction approach," *Int. Scholarly Sci. Res. Innov.*, vol. 3, no. 5, pp. 1070–1078, 2009.

[37] A. I. Ibrahim and H. W. Dommel, "A knowledge base for switching surge transients," presented at the Int. Conf. Power Syst. Trans., Montreal, QC, Canada, 2005.

[38] Z. Zhao, C. Yao, X. Zhao, N. Hashemnia, and S. Islam, "Impact of capacitive coupling circuit on online impulse frequency response of a power transformer," *IEEE Trans. Dielectr. Electr. Insul.*, vol. 23, no. 3, pp. 1285–1293, Jun. 2016.

[39] EEtech Media. (2011). *Parallel Wire Inductance Calculator*, accessed on Sep. 28, 2016. [Online]. Available: http://www.allaboutcircuits.com/tools/parallel-wire-inductance-calculator/

[40] Wikipedia. (2011). *Capacitance*, accessed on Sep. 28, 2016. [Online]. Available: https://en.wikipedia.org/wiki/Capacitance

[41] Wikipedia. (2013). *Transmission Tower*, accessed on Sep. 28, 2016. [Online]. Available: https://en.wikipedia.org/wiki/Transmission_tower

[42] Shenzhen Jixing Wire & Cable Co. (2015). *PVC Insulated Power Cable 6mm^2 Wire*, accessed on Apr. 28, 2016. [Online]. Available: http://jixing.en.made-in-china.com/product/cKaQvosOkPhe/China-PVC-Insulated-Power-Cable-6mm2-Wire.html

[43] Honeywell. (2011). *3-Axis Magnetic Sensor Hybrid HMC2003*, accessed on Apr. 28, 2016. [Online]. Available: https://physics.ucsd.edu/neurophysics/Manuals/Honeywell/HMC_2003.pdf

[44] J. S. Moreno *et al.*, "A non-invasive thermal drift compensation technique applied to a spin-valve magnetoresistive current sensor," *IEEE Sensors J.*, vol. 11, no. 3, pp. 2447–2458, 2011.

[45] C. Reig, S. Cardoso, and S. C. Mukhopadhyay, *Giant Magnetoresistance (GMR) Sensors*. Berlin, Germany: Springer, 2013.

[46] W. E. S. Urquhart. (2013). *General Introduction to Airborne Magnetic Surveys*, accessed on Apr. 28, 2016. [Online]. Available: http://www.geoexplo.com/airborne_survey_workshop.html#introduction

[47] D. Bailey and E. Wright, *Practical SCADA for Industry*. Boston, MA, USA: Newnes, 2003.

[48] S. G. Mallat, "A theory for multiresolution signal decomposition: The wavelet representation," *IEEE Trans. Pattern Anal. Mach. Intell.*, vol. 11, no. 7, pp. 674–693, Jul. 1989.

[49] B. V. P. Mueller. (2005). *Wavelet for Kids*, accessed on Aug. 28, 2016. [Online]. Available: http://gtwavelet.bme.gatech.edu/wp/kidsA.pdf

[50] S.-H. Chen. (2011). *Denoising Using Wavelets*, accessed on Aug. 28, 2016. [Online]. Available: http://www.pws.stu.edu.tw/shchen/Handout/STU_WT_Ch10_Denoise.pdf

[51] S. J. Zhang, "Study on avoiding arc grounding overvoltage by arc suppression coil in Xueying substation," *North China Electr. Power*, vol. 23, no. 3, pp. 23–25, Jul. 2000.

[52] A. A. Girgis, C. M. Fallon, J. C. P. Rubino, and R. C. Catoe, "Harmonics and transient overvoltages due to capacitor switching," *IEEE Trans. Ind. Appl.*, vol. 29, no. 6, pp. 1184–1188, Nov. 1993.

Ke Zhu received the B.E. degree in electrical engineering from China Three Gorges University, Yichang, China, in 2013. He is currently pursuing the Ph.D. degree in electrical and electronic engineering with the University of Hong Kong. His current research and academic interests focus on computational electromagnetics, electric power transmission monitoring, and application of magnetoresistive sensors in smart grid.

Wing Kin Lee received the B.Sc. and M.Sc. degrees from the University of Hong Kong, in 1976 and 1988, respectively, and the M.B.A. degree from the Chinese University of Hong Kong in 1990. He is currently a Senior Teaching Consultant in electrical services and power engineering with the University of Hong Kong. He earned industrial experience while involved with power and communication utility companies in Hong Kong. His current research interests include smart grid demand side management, electrical load signature, and vertical transportation.
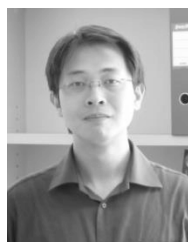
Philip W. T. Pong (SM'13) received the Ph.D. degree in engineering from the University of Cambridge in 2005. He was a Post-Doctoral Researcher with the Magnetic Materials Group, National Institute of Standards and Technology, for three years. In 2008, he joined the Engineering Faculty, University of Hong Kong (HKU), as an Assistant Professor, working on tunneling magnetoresistance sensors and the application of magnetoresistive sensors in smart grid. He is currently a Physicist and an Electrical Engineer with the Department of Electrical and Electronic Engineering HKU, working on magnetoresistive magnetic field sensors and smart grid.